



# Optical Spike Detection and Connectivity Analysis With a Far-Red Voltage-Sensitive Fluorophore Reveals Changes to Network Connectivity in Development and Disease

Alison S. Walker<sup>1,2,3</sup>, Benjamin K. Raliski<sup>1</sup>, Kaveh Karbasi<sup>1</sup>, Patrick Zhang<sup>1</sup>, Kate Sanders<sup>1</sup> and Evan W. Miller<sup>1,2,3\*</sup>

## OPEN ACCESS

### Edited by:

Jeeun Kang,  
Johns Hopkins University,  
United States

### Reviewed by:

Takafumi Inoue,  
Waseda University, Japan  
Adam E. Cohen,  
Harvard University, United States

### \*Correspondence:

Evan W. Miller  
evanwmiller@berkeley.edu

### Specialty section:

This article was submitted to  
Brain Imaging Methods,  
a section of the journal  
Frontiers in Neuroscience

**Received:** 18 December 2020

**Accepted:** 10 March 2021

**Published:** 13 May 2021

### Citation:

Walker AS, Raliski BK, Karbasi K, Zhang P, Sanders K and Miller EW (2021) Optical Spike Detection and Connectivity Analysis With a Far-Red Voltage-Sensitive Fluorophore Reveals Changes to Network Connectivity in Development and Disease. *Front. Neurosci.* 15:643859. doi: 10.3389/fnins.2021.643859

<sup>1</sup> Department of Chemistry, University of California, Berkeley, Berkeley, CA, United States, <sup>2</sup> Department of Molecular & Cell Biology, University of California, Berkeley, Berkeley, CA, United States, <sup>3</sup> Helen Wills Neuroscience Institute, University of California, Berkeley, Berkeley, CA, United States

The ability to optically record dynamics of neuronal membrane potential promises to revolutionize our understanding of neurobiology. In this study, we show that the far-red voltage sensitive fluorophore, Berkeley Red Sensor of Transmembrane potential-1, or BeRST 1, can be used to monitor neuronal membrane potential changes across dozens of neurons at a sampling rate of 500 Hz. Notably, voltage imaging with BeRST 1 can be implemented with affordable, commercially available illumination sources, optics, and detectors. BeRST 1 is well-tolerated in cultures of rat hippocampal neurons and provides exceptional optical recording fidelity, as judged by dual fluorescence imaging and patch-clamp electrophysiology. We developed a semi-automated spike-picking program to reduce user bias when calling action potentials and used this in conjunction with BeRST 1 to develop an optical spike and connectivity analysis (OSCA) for high-throughput dissection of neuronal activity dynamics. The high temporal resolution of BeRST 1 enables dissection of firing rate changes in response to acute, pharmacological interventions with commonly used inhibitors like gabazine and picrotoxin. Over longer periods of time, BeRST 1 also tracks chronic perturbations to neurons exposed to amyloid beta 1–42 ( $A\beta^{1-42}$ ), revealing modest changes to spiking frequency but profound changes to overall network connectivity. Finally, we use OSCA to track changes in neuronal connectivity during maturation in culture, providing a functional readout of network assembly. We envision that use of BeRST 1 and OSCA described here will be of use to the broad neuroscience community.

**Keywords:** action potential, connectivity, neuronal network, spike timing correlation, fluorescent indicators

## INTRODUCTION

Rapid changes in membrane potential, or action potentials, underlie the physiology of the nervous system. Action potential firing depends on both extrinsic and intrinsic factors, many of which are neuronal cell-type specific. Brain function arises not from the behavior of isolated cells but instead from the concerted action of neuronal ensembles, making connectivity between neurons a fundamental prerequisite of neural circuits. The function of any neuronal circuit reflects the heterogeneous activity of its components. Techniques that provide high sampling can give a “voice” to all neuronal types, providing a more representative overview of network function.

Studying neuronal connectivity throughout development increases our understanding of brain circuitry and function, and insights into the mechanisms of neuronal circuit construction may help shed light on how network activity breaks down in aging and disease. Indeed, network dysfunction is a hallmark of neurological diseases, including epilepsy and neurodegenerative disease. An outstanding challenge in these diseases is to define the mechanisms driving network dysfunction. Despite the importance of localizing the where and when of neuronal activity within the context of development, health, and disease, it has been difficult to capture a view of entire network behavior while maintaining cellular resolution.

Part of this challenge is due to limitations in observing and recording network activity in real time with cellular resolution. Electrophysiological techniques are often employed for direct electrical measurements. However, these methods are tedious. Simultaneous recording of multiple neurons is limited to a few neurons per experiment; therefore, information about network interplay is lost. On the other hand, macro-scale brain imaging approaches, including fMRI, positron emission tomography (PET) and EEG, resolve interactions among and between brain regions. However, these approaches cannot provide single-neuron resolution. Studies on the meso-scale, at the level of neuronal circuits but with micrometer spatial resolution, bridge the gap between micro- and macro-scale studies to investigate interactions of neurons within circuits.

Recent studies of functional interactions on the meso-scale rely on multi-electrode arrays (MEAs) which allow simultaneous measurements from tens to thousands of electrodes, or  $\text{Ca}^{2+}$  imaging, which sacrifices a direct measure of electrical activity for the ability to record from large numbers of cells (Chang, 2015). Voltage imaging is an attractive complement to electrode-based recordings and  $\text{Ca}^{2+}$  imaging because it provides a direct readout of electrical changes while maintaining the spatial resolution of light microscopy. Voltage imaging with fluorescent indicators has been a long-standing goal of the scientific community; however, recent developments in both small molecule dyes (Miller et al., 2012; Yan et al., 2012), genetically encoded voltage indicators (Jin et al., 2012; Hochbaum et al., 2014; St-Pierre et al., 2014; Gong et al., 2015; Piatkevich et al., 2018), and combinations of the two (Abdelfattah et al., 2019; Sundukova et al., 2019; Deal et al., 2020) have prompted renewed interest in voltage imaging. Exciting methods are emerging to image large numbers of cultured neurons, but require custom-built

microscopes and high-powered illumination (Werley et al., 2017a,b; Nguyen et al., 2019). Our group has been exploring a complementary approach with voltage-sensitive fluorophores (VoltageFluors) that use photoinduced electron transfer (PeT) as a voltage sensing trigger (Liu and Miller, 2020). VoltageFluors, possess good sensitivity, have fast response kinetics that enable single trial action potential detection, and are bright enough to be imaged with commercially available, low-power LEDs and CMOS cameras. One such VoltageFluor is Berkeley Red Sensor of Transmembrane potential 1, or BeRST 1 (Huang et al., 2015).

In this manuscript, we show that voltage imaging of dissociated hippocampal neurons with BeRST 1 faithfully reports neuronal action potentials across dozens of neurons simultaneously. Along with a semi-automated action potential detection routine, BeRST 1 can rapidly interrogate neuronal excitability and connectivity changes in response to pharmacological manipulation. Finally, we characterize the effects of a pathological challenge, amyloid beta 1–42 ( $\text{A}\beta^{1-42}$ ), on neuronal firing rates and connectivity.

## MATERIALS AND METHODS

### Cell Culture

All animal procedures were approved by the UC Berkeley Animal Care and Use Committees and conformed to the NIH Guide for the Care and Use of Laboratory Animals and the Public Health Policy.

### Rat Hippocampal Neurons

Hippocampi were dissected from embryonic day 18 Sprague-Dawley rats (Charles River Laboratory) in cold sterile HBSS (zero  $\text{Ca}^{2+}$  and zero  $\text{Mg}^{2+}$ ). All dissection products were supplied by Invitrogen, unless otherwise stated. Hippocampal tissue was treated with trypsin (2.5%) for 15 min at 37°C. The tissue was triturated using fire polished Pasteur pipettes, in minimum essential media (MEM) supplemented with 5% fetal bovine serum (FBS; Thermo Fisher Scientific), 2% B-27, 2% 1 M D-glucose (Fisher Scientific) and 1% GlutaMax. The dissociated cells (neurons and glia) were plated onto 12 mm diameter coverslips (Fisher Scientific) pre-treated with PDL at a density of 30–40,000 cells per coverslip in MEM supplemented media (as above). Cells were maintained at 37°C in a humidified incubator with 5%  $\text{CO}_2$ . At 1 day *in vitro* (DIV), half of the MEM supplemented media was removed and replaced with FBS-free media to suppress glial cell growth (Neurobasal media containing 2% B-27 supplement and 1% GlutaMax) (Brewer et al., 1993). Functional imaging was performed on 8–15 DIV neurons to access neuronal excitability and connectivity across different stages of development. References to biological replicates, or “n,” refer to the number of dissections data were collected from.

### VoltageFluor/BeRST 1 Stocks and Cellular Loading

For all imaging experiments, BeRST 1 was diluted from a 250  $\mu\text{M}$  DMSO stock solution to 0.1–1  $\mu\text{M}$  in HBSS ( $+\text{Ca}^{2+}$ ,  $+\text{Mg}^{2+}$ , -phenol red). To load cells with dye solution, the media was first

removed from a coverslip and then replaced with the BeRST-HBSS solution. The dye was then allowed to load onto the cells for 20 min at 37°C in a humidified incubator with 5% CO<sub>2</sub>. After dye loading, coverslips were removed from the incubator and placed into an Attofluor cell chamber filled with fresh HBSS for functional imaging at room temperature (20–23°C).

## Drug Treatments

### TTX, Gabazine, and Picrotoxin Treatments

TTX (Abcam), Gabazine (EMD Millipore), and Picrotoxin (Sigma-Aldrich) were diluted to 1, 10, and 50 μM, respectively in HBSS (+Ca<sup>2+</sup>, +Mg<sup>2+</sup>, -phenol red). Coverslips were loaded with BeRST 1 as outlined in above. After dye loading, coverslips were placed into an Attofluor chamber filled with the Drug-HBSS solutions for functional imaging.

### Amyloid Beta Treatments

Amyloid beta peptides were purchased from AnaSpec and solubilized in a manner analogous to previous protocols (Stine et al., 2003). Briefly, lyophilized peptides were dissolved in 1,1,1,3,3,3-hexafluoro-2-propanol (HFIP) to generate a 1 mM solution. The Aβ-HFIP solution was aliquoted into PCR tubes and evaporated to dryness by placing the open PCR tubes in a chemical fume hood overnight followed by further concentration on a vacuum concentrator. The dried peptide aliquots were then stored over desiccant in glass jars at –20°C. Before addition to the cultures, the dried peptides were re-dissolved to 1 mM in DMSO, vortexed, and sonicated for 10 min. Further dilutions were made with DMSO to 50–500 μM. At 8 DIV, the DMSO stocks were diluted 1:500 in fresh Neurobasal media containing 2% B-27 supplement and 1% GlutaMax (NB++). The Aβ-NB++ solutions were then added to an equal amount of conditioned media on the coverslips to give a total dilution of 1:1,000 for Aβ:Media. The cultures were grown in the Aβ-NB++ solution for 7 days and loaded with dye and imaged at 15 DIV. For vehicle controls, an equal amount of DMSO containing no Aβ was added to the NB++.

## Imaging Parameters

### Spontaneous Activity Imaging

Spontaneous activity imaging was performed on an upright AxioExaminer Z-1 (Zeiss) or an inverted Zeiss AxioObserver Z-1 (Zeiss), both equipped with a Spectra-X light engine LED light (Lumencor), and controlled with Slidebook (3i). Images were acquired using a W-Plan-Apo/1.0 NA 20× water immersion objective (Zeiss) or a Plan-Apochromat/0.8 NA 20× air objective (Zeiss). Images (2048 × 400 px<sup>2</sup>, pixel size: 0.325 × 0.325 μm<sup>2</sup>) were collected continuously on an OrcaFlash4.0 sCMOS camera (sCMOS; Hamamatsu) at a sampling rate of 0.5 kHz, with 4 × 4 binning, and a 631 nm LED (13 mW/mm<sup>2</sup>, SpectraX) with a 631/28 nm excitation bandpass. Emission was collected after passing through a quadruple bandpass dichroic (432/38, 509/22, 586/40, and 654 nm) LP and quadruple bandpass emission filter (430/32, 508/14, 586/30, and 708/98 nm).

### Image Analysis

All imaging analysis was performed using SpikeConnect, a MATLAB script developed in-house to detect action potentials

from fluorescence traces associated with manually drawn regions of interest (ROIs). A brief description of the SpikeConnect workflow is outlined below. This code is available from GitHub at <https://github.com/evanwmiller/spikeconnect>. The code was added to the MATLAB path and can be run on all versions post 2017a. The imaging data was organized in the following manner. Each coverslip was organized into individual folders which contained separate folders for each area imaged on that coverslip. Each area folder contained a brightfield image of the area and the fluorescence movies recorded from that area. All plotting and statistical analysis was performed in GraphPad.

### Drawing Regions of Interest and Labeling Neurons

Individual neurons were labeled by running the function “selectroi\_gui,” selecting a brightfield image (as a tiff file) and importing the movies associated with the image (also as tiff files). The frame rate parameter was set to the recording frame rate. ROIs were drawn around each neuron in the brightfield image and saved. Next, a ROI was drawn around an area of background in the first frame of the fluorescence movie associated with the brightfield image and saved.

### Action Potential Detection

Action potentials (spikes) were detected by running the function “batchkmeans\_gui,” selecting area folders for analysis, and using the background ROI to generate background-corrected fluorescence traces for each neuron ROI. This script then uses k-means clustering, with a cluster number of 3, to identify putative action potentials (spikes), subthreshold events, and baseline. Due to the relative sparsity of action potential firing, the cluster with the fewest points is assigned as “action potentials” and the cluster with the most points is assigned as “baseline” and the indices in time of these activities are extracted. Using a k-means approach means the data is forced into three clusters based on data similarity irrespective of neuronal activity rate. False positives are generated for inactive cells that have zero spikes therefore a signal-to-noise ratio (SNR) threshold is applied by running the function “thresholding\_gui.” SNR was calculated by dividing action potential  $\Delta F/F$  values (calculated as the change in fluorescence intensity from baseline to maximum spike amplitude divided by baseline fluorescence intensity) by the noise (the standard deviation of a sliding window of baseline points, selecting the minimum). Threshold quality control was ensured by comparing the automated spike generation to the raw traces and validated during dual electrophysiology-optical experiments where the optical trace SNR thresholds applied faithfully reproduce the spikes detected by electrophysiology. Homogenous dye loading across multiple neurons meant excellent spike detection was achieved applying a single SNR threshold per coverslip. For example, of the 264 neurons analyzed on control coverslips in **Figure 2**, we found a range of SNR values of 16–19, with a mean value of 18. The spike data was then saved for further analysis.

### Firing Frequency Analysis

Firing frequencies from the spike data were exported as excel files for each ROI by running the function “freqexport\_gui.” The excel files generated contained average frequency (Hz), instantaneous

frequency (Hz), and interspike interval (ms) data for each ROI along with summary columns for each of these three parameters. In this publication, spike timings are represented by interspike interval data. Log transformation is used to reveal patterns of inter spike timings (Reich et al., 2000). This data was then plotted in GraphPad for comparison.

### Area Under the Curve Analysis

Area under the curve (AUC) data was calculated on polynomial flattened  $\Delta F/F$  traces by running the function “auc\_gui” which takes advantage of the MATLAB “Trapz” function to calculate the integral of this vector. The resulting auc data (ms) across the whole trace was then exported as excel files and plotted in GraphPad for comparison.

### Spike Time Tiling Coefficient Analysis

Spike time tiling coefficients (STTC) are the correlation between a pair of spike trains from two neurons (Neuron A and Neuron B, for example) and was developed as a measure of neuronal correlation that is independent of firing rate (Cutts and Eglén, 2014).

$$\text{STTC} = \frac{1}{2} \left( \frac{P_A - T_B}{1 - P_A T_B} + \frac{P_B - T_A}{1 - P_B T_A} \right)$$

$P_A$  is the proportion of spikes from Neuron A which lie within a defined time window ( $\pm \Delta t$ ) of any spike from Neuron B, and  $P_B$  is the proportion of spikes from Neuron B which lie within a defined time window ( $\pm \Delta t$ ) of any spike from Neuron A.  $T_A$  is the proportion of recording/imaging time which is within a defined time window ( $\pm \Delta t$ ) of any spike within a recording session for Neuron A ( $T_B$  is defined similarly). This tiling of the recording time normalizes for firing rate (Cutts and Eglén, 2014). For this study,  $\Delta t = 10$  ms for a window of 20 ms surrounding a single spike. This value was chosen by examining cross correlations of spike timings (Walker et al., 2021). These were calculated by selecting spike data and running the function “sttc\_gui.” The resulting STTC values for each ROI pair were then exported as an excel file and plotted in GraphPad for comparison.

### Electrophysiology

For electrophysiological experiments, pipettes were pulled from borosilicate glass (Sutter Instruments, BF150-86-10), with a resistance of 5–8 M $\Omega$ , and were filled with an internal solution; (in mM) 115 potassium gluconate, 10 BAPTA tetrapotassium salt, 10 HEPES, 5 NaCl, 10 KCl, 2 ATP disodium salt, 0.3 GTP trisodium salt (pH 7.25, 275 mOsm). Recordings were obtained with an Axopatch 200B amplifier (Molecular Devices) at room temperature. The signals were digitized with a Digidata 1440A, sampled at 50 kHz and recorded with pCLAMP 10 software (Molecular Devices) on a PC. Fast capacitance was compensated in the on-cell configuration. For all electrophysiology experiments, recordings were only pursued if the series resistance in voltage clamp was less than 30 M $\Omega$ .

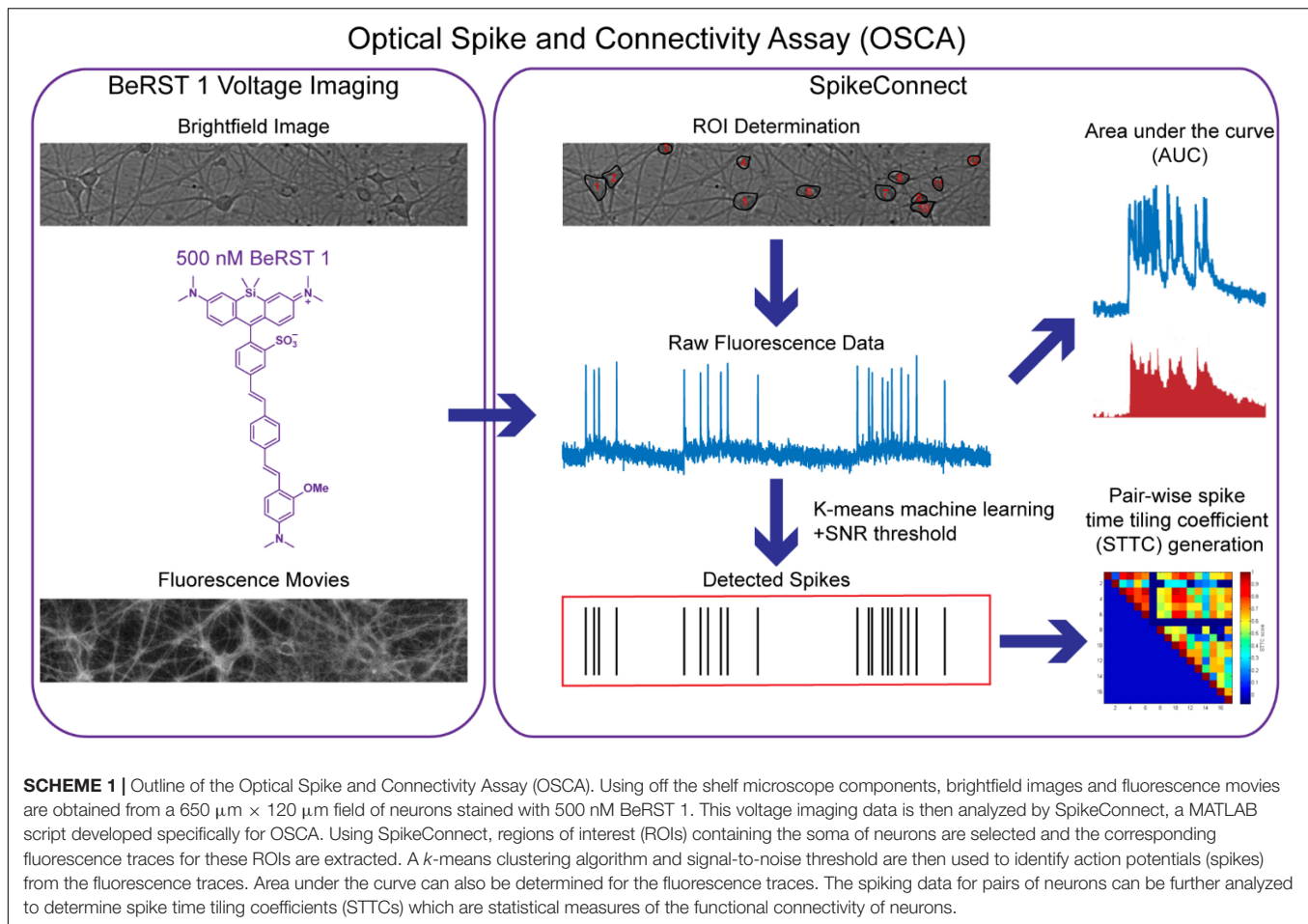
For whole-cell, current clamp recordings in hippocampal neurons, following membrane rupture, resting membrane potential was assessed and recorded at  $I = 0$  and monitored during the data acquisition.

## RESULTS

### Validation of Optical Spike Detection and Analysis With BeRST 1

BeRST 1 is a silicon-rhodamine-based voltage sensitive fluorescent indicator (Huang et al., 2015). We previously reported that BeRST 1 possesses far-red to near infra-red excitation and emission profiles, excellent photostability relative to first-generation voltage sensitive indicators (Miller et al., 2012; Woodford et al., 2015) and linear fluorescence responses to changes in membrane potential. In this study, we further examined the ability of BeRST 1 to report nascent neuronal activity and connectivity in cultured rat hippocampal neurons (**Scheme 1**). In order to maximize SNRs for longer recordings of spontaneous activity, we assessed combinations of light power and BeRST 1 concentration that could be tolerated before disruption of action potential firing was observed. We evoked action potentials (using field stimulation) while imaging for 30 s in neurons loaded with BeRST 1 (**Supplementary Figures 1a,b**). We examined illumination intensities ranging from 6.5 mW/mm<sup>2</sup> to 70 mW/mm<sup>2</sup> at both 500 nM and 1  $\mu$ M BeRST 1 loading concentration (**Supplementary Figures 1c,d**). We find that similar SNR values can be achieved with either 500 nM or 1  $\mu$ M BeRST 1 loading (**Supplementary Figure 1e**). However, at 1  $\mu$ M BeRST 1 loading, a high proportion of neurons displayed a sudden rise in baseline fluorescence (**Supplementary Figure 1b**, upper), rapid oscillations in the baseline (**Supplementary Figure 1b**, middle), or sudden steps or jumps in the baseline fluorescence (**Supplementary Figure 1b**, lower). These dynamic baseline fluorescence shifts were often followed by variability in action potential amplitudes, morphologically observed cellular granulation and inactivity, and were therefore postulated to be an early indicator of cell death. We labeled these neurons “unhealthy” (**Supplementary Figure 1b**) and any neurons that showed uniformly flat baselines as “healthy” (**Supplementary Figure 1a**). This extracellular stimulation configuration was used to configure “safe” light power and dye concentration combinations. We found that for the same SNR, phototoxicity (scored as non-linear changes in baseline fluorescence) was observed less when using a lower dye concentration (500 nM), even at higher illumination intensity (up to 40 mW/mm<sup>2</sup>), while at high dye concentration (1  $\mu$ M), even low light intensity (17 mW/mm<sup>2</sup>) could result in baseline fluorescence shifts (**Supplementary Figure 1d**). Bath application of 500 nM BeRST 1 excited at up to 30–40 mW/mm<sup>2</sup> provided stable optical recordings for > 20 s (limited by the large file sizes generated). We therefore used an illumination intensity of 13 mW/mm<sup>2</sup> for all the recordings in this study, to stay well below the threshold at which we began to observe disruption to action potential recordings. Following loading, BeRST 1 localized to the plasma membranes of cell bodies and processes (**Figures 1a,b**) with neuronal somatic ROIs producing traces that show fast depolarizations that occur randomly in time.

A challenge in recording spontaneous, as opposed to evoked activity, is spike detection. While principal/independent component analysis (PCA-ICA) analysis techniques are often

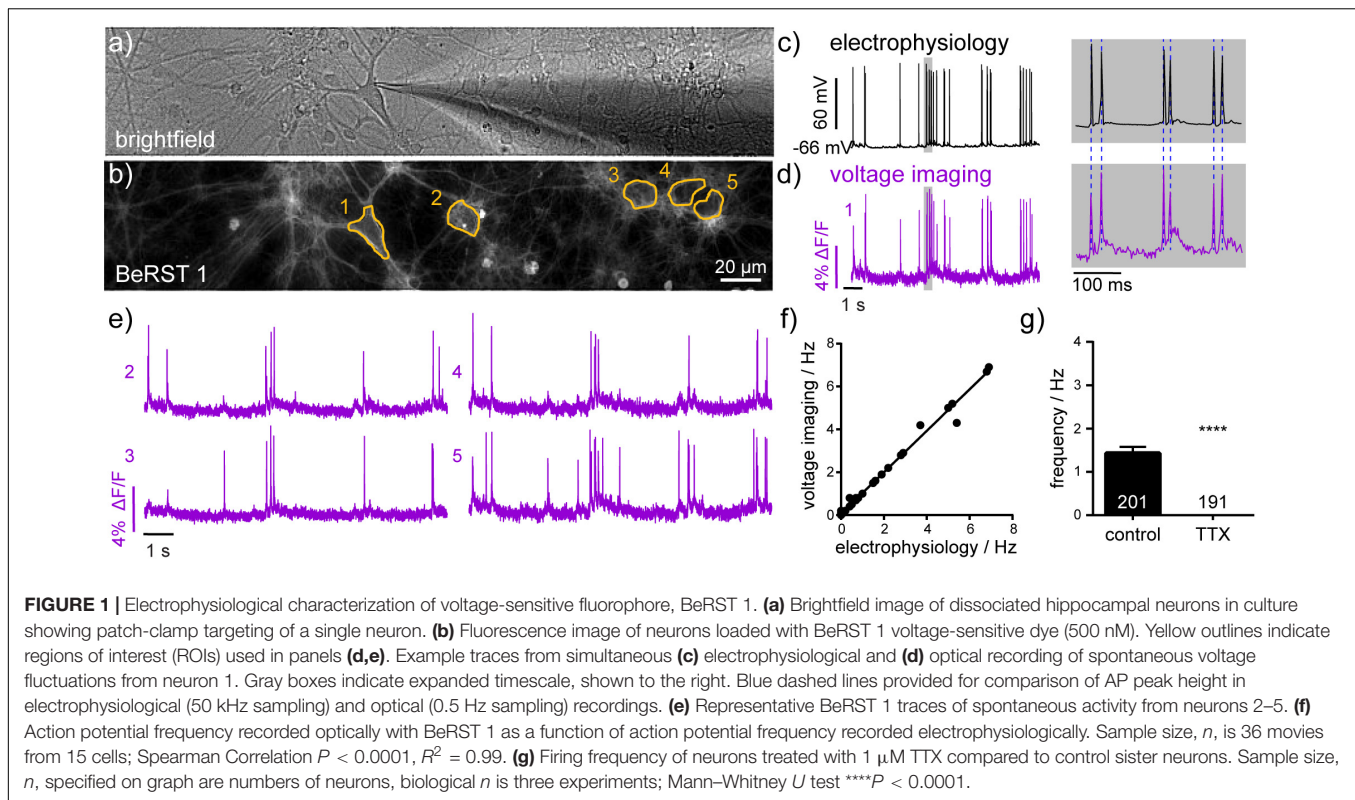


applied to analyze large functional imaging datasets (Hill et al., 2010; Frady et al., 2016), they spatially segment neurons based on activity profiles, thereby omitting silent/quiescent neurons, which are important circuit components (Ovsepian, 2019). An imaging approach enables identification of neurons vs. non-neurons via morphology in a transmitted light image and can be confirmed with immunocytochemistry (Walker et al., 2021). We developed an ROI-based semi-automated routine for action potential detection in MATLAB, which we call SpikeConnect. After manual image segmentation, or ROI selection, SpikeConnect uses a k-means (MacQueen, 1967; Xu and Tian, 2015) unsupervised clustering (Kiselev et al., 2019) algorithm to separate intensity values into three separate groups (see sub-section “Action Potential Detection” in “Materials and Methods” section). A signal to noise threshold (see sub-section “Action Potential Detection” in “Materials and Methods” section) is set and spike timings extracted for each action potential from every neuron recorded. We added additional modules to SpikeConnect to calculate other metrics from the fluorescence traces including the AUC, and the STTC (Cutts and Eglén, 2014) between pairs of spike trains to determine network connectivity, which will be addressed in further detail later in the manuscript.

To assess the utility of BeRST 1 voltage imaging coupled with SpikeConnect algorithms to detect somatic action potentials we compared BeRST 1 optical signals with simultaneously

recorded electrophysiological traces using whole-cell patch-clamp electrophysiology (Figures 1c,d). A plot of action potential frequency recorded optically and analyzed with SpikeConnect vs. frequency measured with electrophysiology and analyzed with Clampfit software reveals a near-perfect correlation between the imaging and electrode approach (Figure 1f, comparisons across 36 recordings/movies from 15 different cells,  $R^2 = 0.99$ ) confirming BeRST 1 imaging, in combination with SpikeConnect analysis, faithfully reports action potentials during bouts of spontaneous activity. While the SNR of the whole-cell, patch-clamp recording is superior to the optical BeRST 1 recording, BeRST 1 readily resolves action potentials and sub-threshold events (Figures 1c,d) and can do so from multiple cells simultaneously (Figure 1e). The small jitter in optical action potential height (Figure 1d) relative to the patch-clamp recording (Figure 1c) is likely a result of the lower optical sampling rate (500 Hz) relative to the electrophysiology (50 kHz). In addition, treatment of cultures with the action potential blocker, sodium channel antagonist tetrodotoxin (TTX,  $1 \mu\text{M}$ ,  $n = 191$  neurons), completely abolished spontaneous action potential activity recorded optically (Figure 1g).

In summary, combining BeRST 1 voltage imaging with SpikeConnect algorithms, otherwise known as optical spike and connectivity assay (OSCA), enables detection of spontaneous action potential firing with similar confidence to gold-standard



electrophysiological techniques. Our voltage imaging approach dramatically increases throughput compared to patch-clamp electrophysiology. The combination of precise electrical readout of action potentials on fast temporal scales with improved throughput places OSCA in a position to evaluate changes in activity across neuronal networks following both pharmacological and pathophysiological modulations.

### Characterization of Hyperactivity Following Pharmacological Modulation

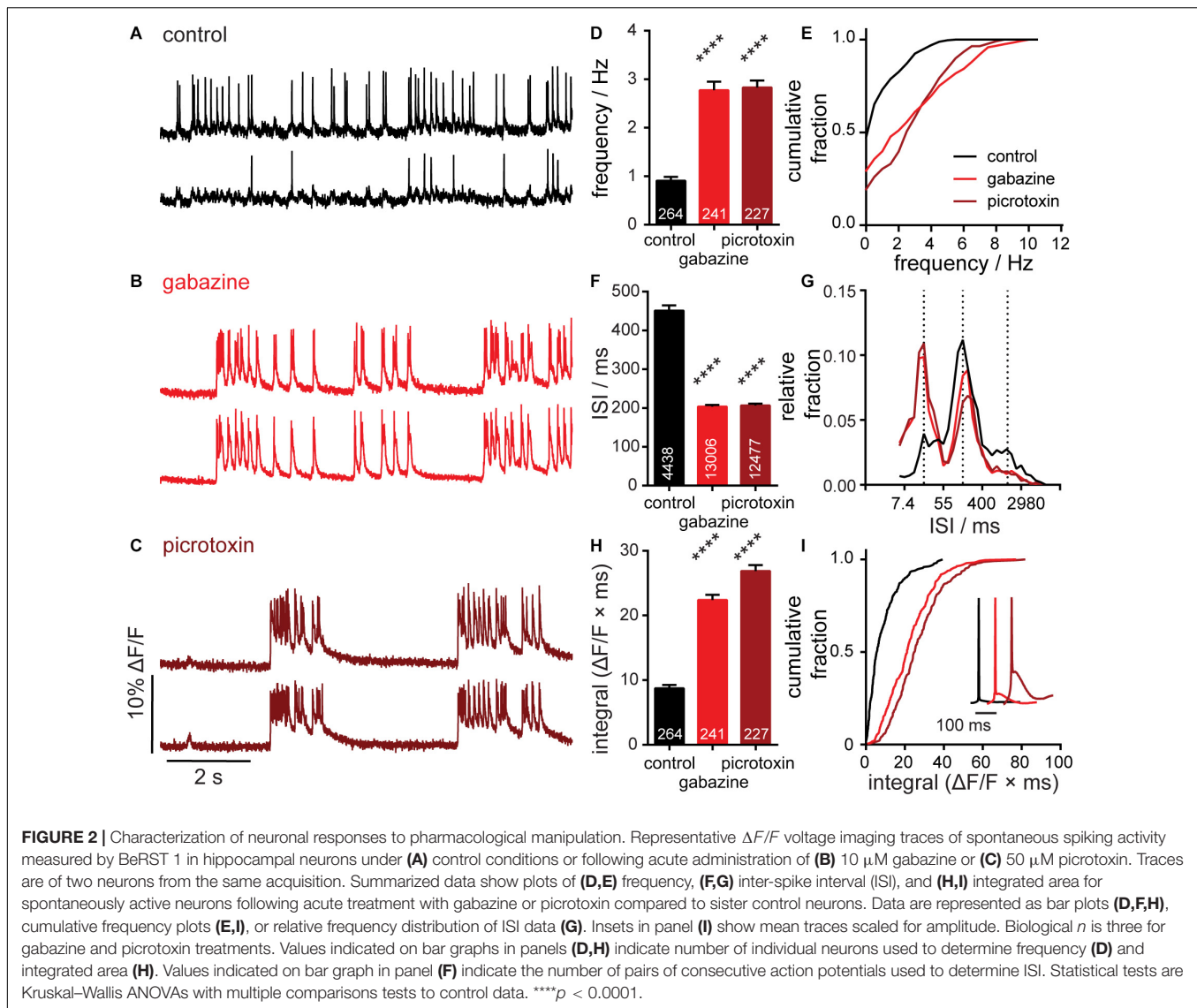
First, we wanted to test the utility of OSCA to detect pharmacological modulators which could enhance neuronal activity. Hippocampal dissociated cultures are highly connected and show spontaneous and synchronous activity in basal conditions (**Figure 1**), and provide a powerful model system for the induction of epileptic activity (Furshpan and Potter, 1989; Vedunova et al., 2013). A simple way to achieve this is to block the activation of ionotropic GABA<sub>A</sub> receptors, which generate inhibitory postsynaptic potentials (IPSCs) during synaptic transmission. This phasic inhibition is both essential in preventing overexcitation, leading to pathological states, as well as generating rhythmic activities in neuronal networks (Farrant and Nusser, 2005).

We treated 14–17 DIV hippocampal cultures for 20 min with vehicle or gabazine (GBZ, 10  $\mu\text{M}$ ), a competitive GABA<sub>A</sub>R antagonist or picrotoxin (PTX, 50  $\mu\text{M}$ ), a non-competitive inhibitor preferentially interacting with agonist-bound GABA<sub>A</sub>Rs (Newland and Cull-Candy, 1992). The high SNR and throughput of OSCA allowed us to rapidly isolate action potentials for 732 neurons. We found that treatment with

either gabazine or picrotoxin results in a nearly 3-fold increase in mean firing frequency (**Figure 2D**). Control, untreated, cultures fired at a rate of 0.9 Hz ( $\pm 0.08$  Hz, SEM), gabazine-treated cultures at 2.8 Hz ( $\pm 0.2$ , SEM), and picrotoxin-treated cultures at 2.8 Hz ( $\pm 0.1$ , SEM). Consistent with network-wide lifting of synaptic inhibition, the distribution of action potential frequencies shifts to higher frequencies (**Figure 2E**). Inhibitor-treated neurons show a decrease in the proportion of quiescent neurons, indicated by a change in Y-intercept of the cumulative frequency from approximately 47% of neurons quiescent in control cultures to 29% in gabazine- and 19% in picrotoxin-treated cultures (**Figure 2E**).

For defined imaging periods, increases in frequency correspond to decreases in inter-spike interval (ISI). We observed that treatment with GBZ and PTX significantly decreased ISI when compared to vehicle control (**Figure 2F**). Examining the distribution of ISI values gives insight into patterns of spike timings, synchrony, and network organization (**Figure 2G**). Using OSCA, we find that action potentials occur within three discrete timing bands in control cultures: at ISI intervals of 20 ms ( $\sim 50$  Hz), 150 ms ( $\sim 6.6$  Hz), and 1,100 ms ( $\sim 0.9$  Hz). In the presence of GBZ and PTX, the three timing bands are maintained, but inhibitor treatment evokes a redistribution in the proportion of activity within each band. High frequency ( $\sim 50$  Hz) firing increases 2.5 fold, balanced by a 30–40% decrease in moderate firing ( $\sim 6.6$  Hz) and 50% decrease in slow firing ( $\sim 0.9$  Hz) frequencies (**Figure 2G**).

GABA<sub>A</sub>R inhibition produces periods of sustained depolarization with APs riding on top (**Figures 2B,C**). These waveforms are highly reminiscent of paroxysmal depolarizing



shifts (PDS), an electrical hallmark of “ictal-like” epileptic activity (Hablitz, 1984). To quantify this activity, we calculated the response integral, or AUC using a custom module within SpikeConnect and found that acute gabazine and picrotoxin treatment more than doubles the  $\Delta F/F$  integral (Figure 2H). The cumulative frequency plot emphasizes the magnitude of the shift: 70% of control neurons show spikes that return to baseline with integrals  $< 10 \Delta F/F/\text{ms}$ , whereas only a small proportion do with GABA<sub>A</sub>R blockade (GBZ, 15%; PTX  $< 10\%$ , Figure 2I). Interestingly, while changes in frequency and ISI are highly reproducible between GBZ and PTX (Figures 2D–G), we find that PTX treatment provokes larger sustained depolarizations than GBZ (Figure 2I, inset, dark red vs. red). This might be due to the ability of PTX, but not GBZ, to block tonic inhibition, a mode of persistent shunting inhibition mediated by extrasynaptic GABA<sub>A</sub>R activity, which depresses excitatory postsynaptic potentials (EPSPs) (Farrant and Nusser, 2005). It is possible that the release of

tonic inhibition by PTX leads to the generation of larger EPSPs, in turn causing greater activation of downstream effectors including voltage-dependent calcium channels thought to underlie sustained depolarization states in PDS generation (Kubista et al., 2019).

Together, these data show that OSCA is highly amenable to the dissection of neuronal activity following global, acute network disinhibition, phenotypically capturing several hallmarks of epilepsy-like activity. In addition to robust detection of activity changes at the neuronal level, the ability to record concurrently from large numbers of neurons enabled additional insights into network-wide effects, including redistribution of spike timings. Disinhibition of a neuronal network represents a major pharmacological intervention that robustly increases neuronal activity, and while generating a robust seizurogenic model in vitro, such events are rarely observed under physiological conditions. To determine whether OSCA could offer insight into a milder network challenge, we sought to study the effects

of a pathophysiological challenge by A $\beta$  on neuronal and network activity.

## Pathophysiological Modulation With A $\beta^{1-42}$ Induces Neuronal Hyperactivity

Network dysfunction is a common feature of neurodegenerative disease. In Alzheimer's disease (AD), the most common neurodegenerative disease, network dysfunction, or epileptiform activity, has been observed in AD patients (Sperling et al., 2009; Huijbers et al., 2015) and mouse models (Palop et al., 2007) which simulate AD. One of the hallmarks of AD is an accumulation of A $\beta$  plaques within the brain. When applied chronically, A $\beta$  induces synaptic dysfunction and disrupts network connectivity (Peña et al., 2006). To study network dysfunction in AD models a plethora of available methods for recording activity have been adopted, all with their inherent limitations, often in throughput or spike resolution (Busche et al., 2012; Verret et al., 2012; Ciccone et al., 2019; Zott et al., 2019). As an area of vital and active research, we wanted to examine the utility of BeRST 1 voltage imaging, to dissect the impact of A $\beta$  on neuronal network function in high detail.

Chronic exposure of developing hippocampal cultures to varying concentrations of A $\beta^{1-42}$  (50 nM to 1  $\mu$ M, **Figures 3B,C**) for 7 days increases neuronal firing frequency in a dose-dependent manner, reaching an almost 2-fold increase following treatment with 1  $\mu$ M A $\beta^{1-42}$  (**Figure 3D**). Interestingly, we do not observe a change in the number of quiescent neurons, which remains constant at approximately 50% across all A $\beta^{1-42}$  treatment conditions and control (**Figure 3E**), and suggests a mechanism where excitable cells are more active following prolonged exposure to A $\beta^{1-42}$ . This result contrasts with the network-wide increase in spiking neurons seen with acute GABA<sub>A</sub>R inhibitor treatment (**Figure 2E** vs. **Figure 3E**). The ISI for neurons treated with A $\beta^{1-42}$  decreases relative to controls, consistent with an increase in activity upon A $\beta^{1-42}$  treatment (**Figure 3F**). Examination of the distribution of ISI values again reveals bands of spike timings clustered around values of 20, 150, and 1,100 ms (50, 6.6, and 0.9 Hz, respectively; **Figure 3G**). The shape of the ISI distributions in response to A $\beta^{1-42}$  does not change significantly, indicating that the gross firing patterns in the A $\beta^{1-42}$ -treated cultures remain similar to controls. A $\beta^{1-42}$  exposure causes a modest increase in the integrated response with no overt alterations to the shape of mean action potentials (**Figures 3H,I**).

Taken together, these data show that chronic treatment with >500 nM A $\beta^{1-42}$  causes hyperactivity with significant increases in frequency and  $\Delta F/F$  integral and decreased ISI (**Figure 3**). The magnitude of these effects, while significant, are more subtle compared to acute GBZ and PTX (**Figure 2**) but still readily detected by OSCA. Interestingly, hyperactivity following A $\beta^{1-42}$  treatment manifests differently compared to GABA<sub>A</sub>R blockade: chronic A $\beta^{1-42}$  treatment gives no change in fraction of quiescent neurons (**Figure 3E**) or redistribution of ISI values (**Figure 3G**). Chronic A $\beta^{1-42}$  treatment, unlike acute GABA<sub>A</sub>R blockade, does not appear to alter the gain (or excitability) across the entire network. Rather, it appears that already-active

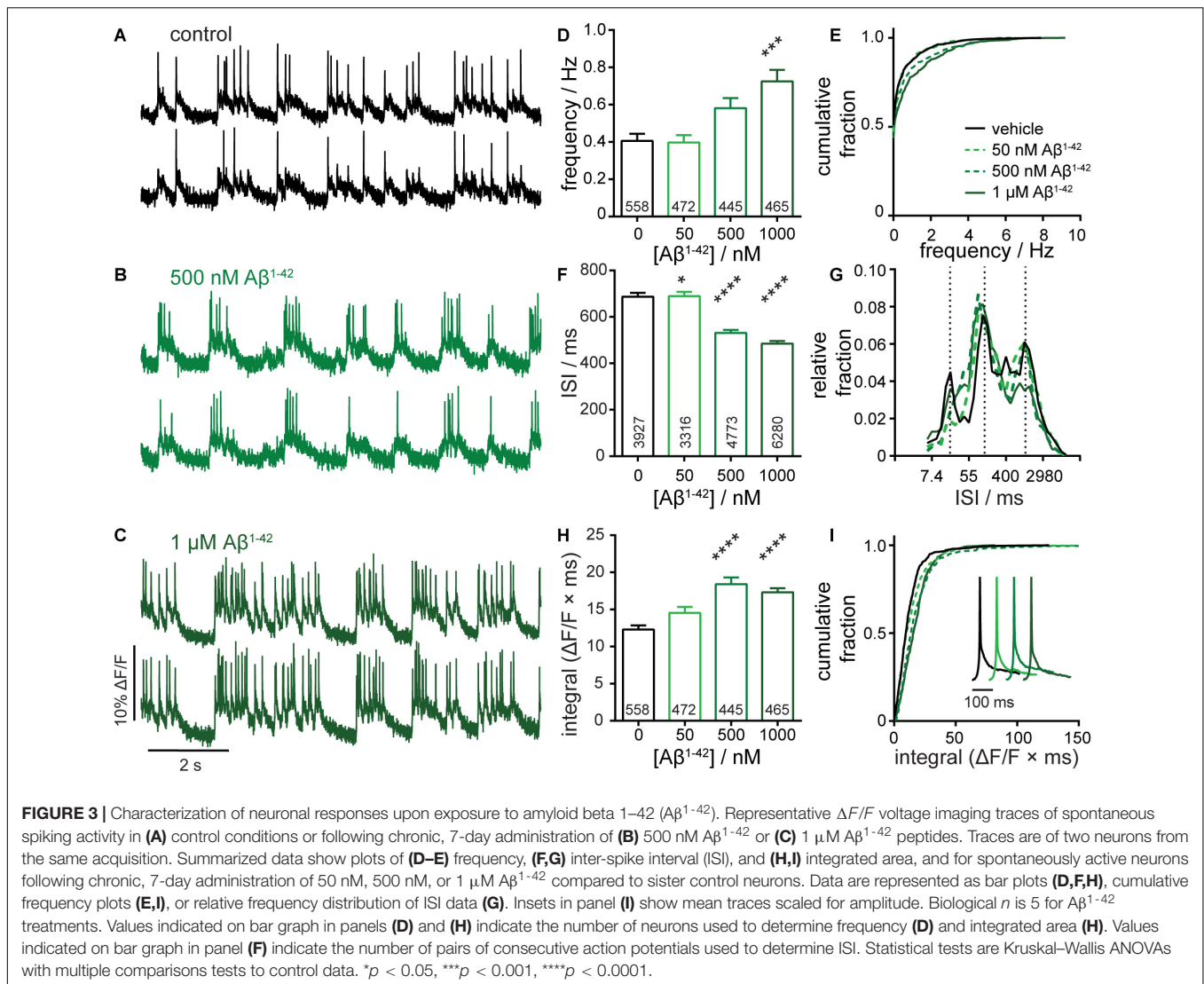
neurons become more active, suggesting a change in underlying network connectivity. Therefore, we applied a statistical measure of functional connectivity to OSCA-detected spike trains to explore this idea further.

## Functional Characterization of Network Formation During Development

The precise timing of action potential firing between different neurons in circuits underpins the workings of the nervous systems; therefore to develop a more comprehensive picture of neural circuits, we must move away from studying single neurons in isolation, and shift toward a more holistic study of circuits (Yuste, 2015). OSCA allows us the opportunity to infer network connectivity by evaluating temporal spiking relationships between neurons recorded simultaneously. Here, we applied a statistical method of quantifying functional connectivity, the STTC, to the precise spike timings of clusters of neurons recorded simultaneously (10–25 neurons per field of view). Among possible descriptors of neuronal correlation (Cutts and Eglén, 2014), STTC is attractive because it resists the influence of confounding variables, including firing rate by “tiling” the recording session and only examining spikes in Neuron A that lie within a defined time window ( $\pm 10$  ms) of spikes in Neuron B (Cutts and Eglén, 2014), thus enabling a more reliable assessment of correlation for networks of heterogenous cell types. STTC ranges from +1 (complete correlation) and  $-1$  (negative correlation).

To validate the use of STTC in a voltage imaging context, we took advantage of the stereotyped structural and functional maturation, or development, of synapses in dissociated hippocampal cultures (Dotti et al., 1988; Wagenaar et al., 2006). In the dissociated neuron culture model, action potentials emerge as early as 4 DIV, but synapse formation doesn't begin in earnest until 8–10 DIV (Basarsky et al., 1994; Grabrucker et al., 2009). Synapse formation initially leads to an excess of functional connections which over the following days are pruned in a period of synaptic remodeling to generate an efficient neuronal network with a set-point of activity (Goda and Davis, 2003; Südhof, 2018).

Using OSCA, we monitored neuronal activity in rat hippocampal neuron cultures at 8, 12, and 15 DIV, assessing the evolution of activity over the course of 1 week of growth and development in vitro. We found that overall neuronal firing frequency did not scale linearly with the developmental age of neuronal cultures (**Figure 4A**). Rather, spiking rates peaked at 12 DIV before decreasing at 15 DIV (**Figure 4A**). In fact, examining the firing frequency alone indicates no difference between neuronal activity at 8 and 15 DIV, with the distribution of firing frequencies perfectly overlying (**Figure 4B**, light blue vs. black). However, analysis of network STTC scores reveals robust changes (**Figures 4C,D**). We find that STTC and network connectivity increases step-wise over the 7 day period, regardless of the underlying firing rate (**Figures 4C,D**). Generation of synchronous activity plays central roles in fine-tuning connectivity during CNS development. We find



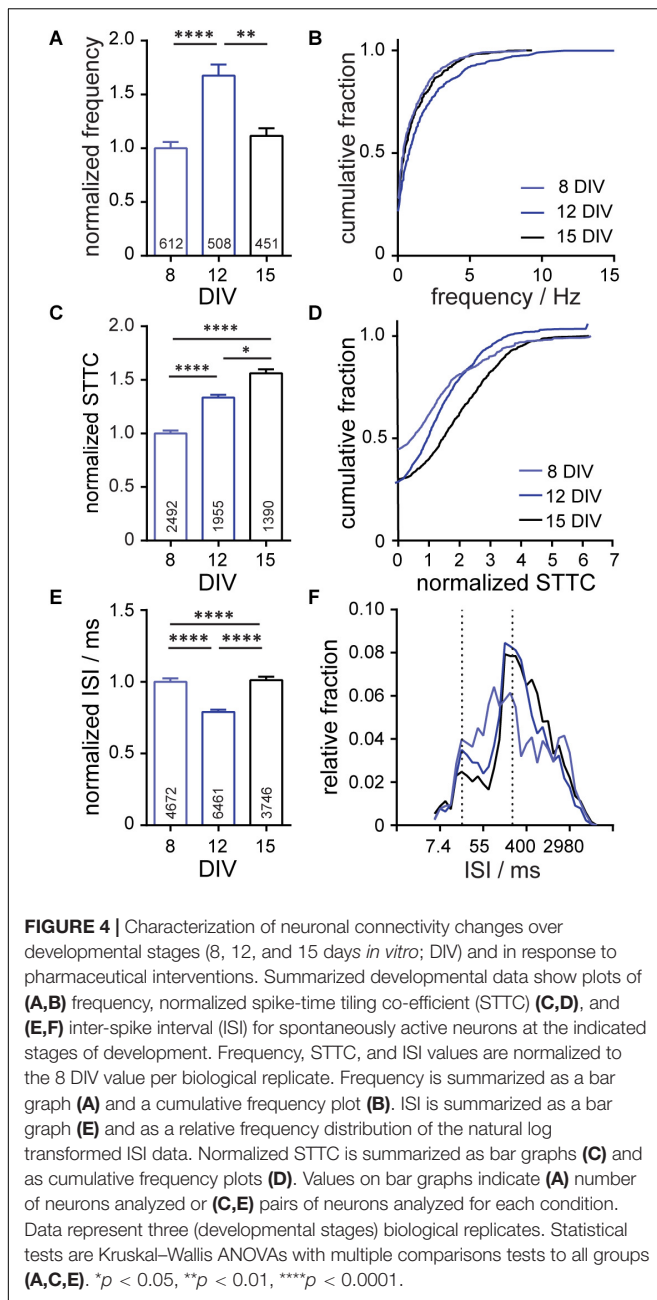
this reflected in the ISI with spike timings occurring across a broad range of intervals at 8 DIV (Figures 4E,F, light blue) before sharpening into defined bands of activity with increasing maturation at DIV 12 (Figures 4E,F, blue) and DIV 15 (Figures 4E,F, black). These data show empirically that over time, neuronal networks modulate their firing rates, neuron-neuron connectivity, and network synchronicity, consistent with the idea that, at early time points during the development of synapses and networks in culture, neurons form an excess of synapses, overshooting a homeostatic set-point, which might then be restored after synaptic pruning (Goda and Davis, 2003; Südhof, 2018).

### Chronic Exposure to $A\beta^{1-42}$ Induces Changes to Neuronal Connectivity

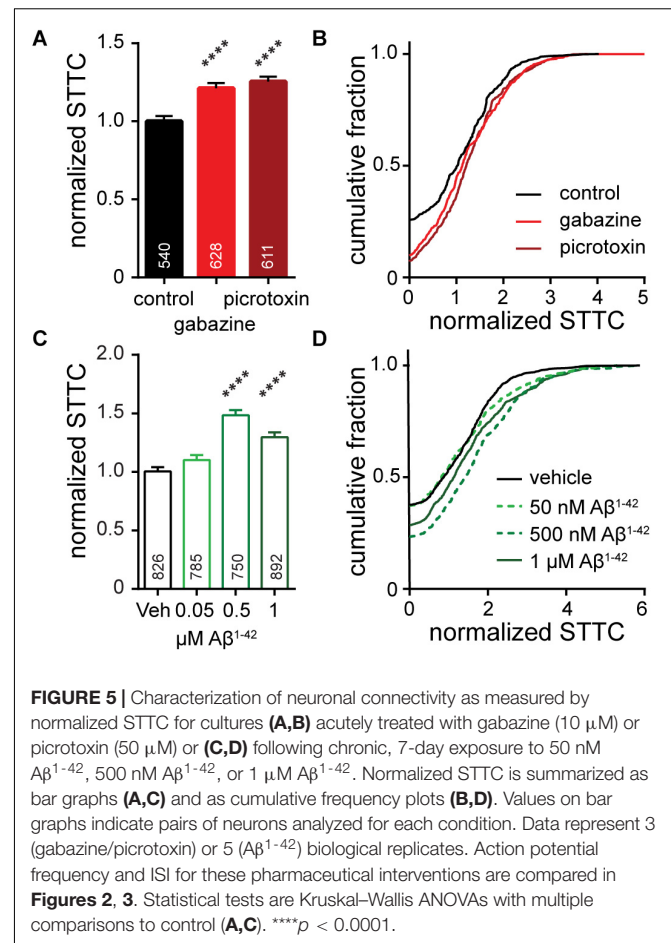
To determine whether perturbations to neuronal networks, GABA<sub>A</sub>R blockade and  $A\beta^{1-42}$  treatment, would manifest changes in neuronal correlation, we analyzed network STTC.

As expected, acute network-wide disinhibition with GBZ and PTX (as in Figure 2) increased network synchrony: STTC values increase compared to control cultures (Figures 5A,B). This is consistent with releasing the inhibitory brake on the system so that multiple neurons downstream of excitatory synaptic drivers are more likely to fire and are therefore more co-ordinated. However, the observed increase in STTC for GABA<sub>A</sub>R blockade is relatively small (20–30% increase) compared to the nearly 300% increase in firing frequency observed for the same treatment (Figure 2). This indicates that while correlation between spike trains does increase, changes in network inter-connectivity are not a key contributor to the frequency changes under acute, global disinhibition.

For chronic treatments with  $A\beta^{1-42}$  (Figure 3), we also observed increases in network synchrony. Low concentrations of  $A\beta^{1-42}$  (50 nM) have little effect on either firing rate (Figure 3D) or relative STTC (Figures 5C,D). However, intermediate concentrations of  $A\beta^{1-42}$  (500 nM) produce a



nearly 50% increase in STTC and a 25% increase at 1  $\mu\text{M}$  (Figures 5C,D). Interestingly, compared to treatment with either GBZ or PTZ (Figure 2),  $\text{A}\beta^{1-42}$  exhibits milder effects on firing frequency, integral, and ISI (Figure 3) but larger changes to the STTC value relative to controls (25 to 50% increase in STTC, Figures 5C,D). Together with frequency data showing no change to the number of unresponsive neurons (Figure 3E), the increase observed in STTC points to a mechanism where active neurons, under chronic exposure to  $\text{A}\beta^{1-42}$ , increase the number or strength of existing connections in downstream neurons.



## DISCUSSION

In this manuscript, we demonstrate the utility of OSCA, a voltage-sensitive fluorophore-based imaging and analysis approach in dissociated hippocampal neurons, to (1) provide high fidelity tracking of action potentials across large numbers of neurons, (2) quantify hyperactivity following pharmacological and pathophysiological network modifications, (3) validate a statistical measure of functional connectivity (Spike-Time Tiling Co-efficient; STTC), and (4) apply STTC to understand network organization in pharmacologically and pathophysiological modified circuits.

## OSCA Reliably Reports Activity Within Neuronal Networks

In this study, we show that OSCA delivers detailed information on action potential firing frequency with the same resolution as the gold-standard technique for this metric, patch clamp electrophysiology (Figure 1). Moreover, we demonstrate that OSCA can robustly detect network silencing (Figure 1) and neuronal hyperactivity driven by either pharmacological (Figure 2) or pathological agents (Figure 3). However, where patch clamp is low-throughput and limited in the number of neurons recorded, OSCA is advantageous as it enables the

recording of firing frequency and ISI in larger numbers of neurons simultaneously. The ability to simultaneously record from multiple cells enables OSCA to minimize cell-type bias and to gain holistic overviews of heterogeneous hippocampal networks *in vitro* by examining activity distributions. For example, in developing cultures (8 DIV), we found that spike intervals were distributed across the whole range of resolvable frequencies (0–150+ Hz), but when mature, at > 12 DIV, active neurons settled into three main bands of ISI centered around: 20 ms (~50 Hz), 150 ms (~6.6 Hz) and 1,100 ms (~0.9 Hz) (**Figure 4F**). Although the number of active neurons within each frequency band was redistributed after pharmacological disinhibition of the network (**Figure 2**), the maintenance of the three activity bands suggests that these patterns of neuronal activity are not acutely controlled by inhibition.

## OSCA Enables Assessment of Functional Connectivity Within Networks

Neuronal connectivity in dissociated cultures cannot easily be assessed by patch clamp electrophysiology. Instead, neuronal connectivity is often assessed using MEA which, while powerful at describing dynamic states, often use global activity such as bursts or activity complexity occurring in a proportion of electrodes simultaneously (Hyvärinen et al., 2019) because ascribing single spikes to single neurons is challenging. Using an optical approach, spatial resolution is vastly improved, enabling us to confidently attribute activity signatures to individual neurons. After recording from multiple cells simultaneously, we quantified the connectedness of the underlying network using STTC, a statistical measure (STTC) of functional connectivity. As validation of this metric, we observed clear stepwise increases in functional connectivity as networks matured *in vitro*, undergoing organization and synchronization coincident with synapse formation and refinement (**Figure 4**). These data are also consistent with MEA studies of development in cultured neurons (Wagenaar et al., 2006). After pharmacological disinhibition of the network with GABA<sub>A</sub>R blockers, we observed a further increase in STTC over control conditions representing an increase in network synchrony (**Figure 4**). Together these data show that STTC is a useful readout for defining network connectivity in voltage imaging.

## Aβ<sup>1–42</sup> Challenge Enhances Neuronal Firing Frequency and Connectivity

Understanding of the role of Aβ in modulating neuronal function is constantly evolving. Models with elevated levels of Aβ have described synapse loss, hypoactivity, and neuronal death coinciding with cognitive decline (Shankar and Walsh, 2009). However, it is becoming increasingly evident that hyperactivity characterized by epileptiform activity is a hallmark of pre-clinical and early stage AD (Sperling et al., 2009; Huijbers et al., 2015) and is also observed in mouse models simulating AD (Palop et al., 2007). Using OSCA, we show that chronic (7 day) treatment of hippocampal cultures with > 500 nM Aβ<sup>1–42</sup> peptide resulted in increased neuronal firing frequency (**Figure 3**)

and an increase in network correlation as measured by STTC (**Figure 4**). These data link exposure to Aβ<sup>1–42</sup> with neuronal hyperactivity, consistent with Ca<sup>2+</sup> imaging data (Busche et al., 2012). Several mechanisms have been proposed to underlie Aβ-mediated neuronal hyperactivity, including impaired glutamate reuptake (Zott et al., 2019), reduced function of interneurons (Palop et al., 2007; Palop and Mucke, 2016), changes in neurotransmitter release probability (Abramov et al., 2009; Wang et al., 2017) and intrinsic excitability (Ciccone et al., 2019). However, without a detailed mechanistic study, it is difficult to extrapolate effects on specific intrinsic or synaptic properties to the working of microcircuits. Here, we uncovered that relatively modest increases in firing frequency following Aβ<sup>1–42</sup> treatment were accompanied by robust increases in STTC, suggesting a network that is more organized with higher levels of synchrony (**Figures 3, 4**). While the role of hyperactivity in AD is still to be fully elucidated, it may play compensatory and/or neuroprotective roles within the network (Elman et al., 2014).

## Looking to the Future: Limitations and Future Directions

Voltage imaging methods have improved over the last decade, beginning to address problems of poor signals, slow temporal kinetics, and cytotoxicity. BeRST 1 combines these improvements with ease of use and widespread applicability: optical voltage recordings can be made using commercially available, off-the-shelf imaging equipment and without the need for genetic modifications to the sample.

One drawback to a small molecule fluorophore approach to voltage imaging is the lack of cell-type selectivity afforded by genetically encoded approaches (Lin and Schnitzer, 2016). In the case of OSCA, this can be mitigated during ROI selection via brightfield images, where morphology informs selection of neurons, avoiding glia and other non-neuronal cells; however, staining of membranes of glia and non-neuronal cells contributes to background fluorescence, eroding  $\Delta F/F$  and SNR, making detection more difficult. For further cell-type specificity, OSCA and voltage imaging with BeRST can be paired with post-hoc fixation an immunostaining to classify and segregate neurons from non-neurons and even identify neuronal sub-types (Williams Megan et al., 2011; Walker et al., 2021). In the future, chemical-genetic (Liu et al., 2017; Grenier et al., 2019; Ortiz et al., 2019; Deal et al., 2020) and cell-type specific targeting (Fiala et al., 2020) could be employed with OSCA analysis to achieve cell-type specific imaging with small molecule reporters.

The recent expansion of available voltage sensitive indicators presents new challenges in analysis of voltage imaging datasets, which, compared to Ca<sup>2+</sup> imaging data, are generally larger in size, contain smaller indicator pools defined by a cell membrane rather than a cytosol, and possess smaller and shorter fluorescence transients (Kulkarni and Miller, 2017). Our data analysis approach, which relies on selection of ROIs, followed by k-means clustering for spike detection, complements existing methods of analysis (Hill et al., 2010; Frady et al., 2016) which rely on PCA/ICA to define activity and ROIs. A number of emerging

methods for analysis of voltage imaging data should be applicable for voltage imaging with BeRST and related indicators (Buchanan et al., 2019; Cai et al., 2020; Xie et al., 2020).

The ability of OSCA to robustly detect changes in network activity profiles, coupled with the flexibility of utility in neuronal culture preparations from any host species or preparation, especially those where genetic manipulation is impossible, cumbersome, or expensive, such as patient-derived human induced pluripotent stem cell-derived neurons (Williams et al., 2019; Puppo et al., 2021), make this technique directly amenable for high-throughput screening. In recent years, there has been a resurgence in phenotypic screening for discovering new drug candidates, drug targets and for neurotoxicological testing, with a focus on *in vitro* models that translate to *in vivo* and ultimately the clinic (Moffat et al., 2017). The VoltageFluor dyes based on fluorescein have been used in human stem-cell derived neurons (Adil et al., 2017a,b; Kulkarni et al., 2017; Rodrigues et al., 2017), and more recent studies have used BeRST 1 in human iPSC-derived neurons (Puppo et al., 2021), both systems with great disease modeling potential. While limitations exist for the use of cultured neurons as a model system for intact brains, the reduced complexity of *in vitro* models using cultured neurons make them a useful point of departure for dissecting cellular and molecular cues that are important for proper neuronal function (Turrigiano et al., 1998; Burrone et al., 2002; Williams Megan et al., 2011) and assessing the effects of pharmacological intervention on these phenotypes. Pairing OSCA with human iPSC-derived disease models will be a powerful avenue for future research, generating large functional datasets with greater translatability to humans.

## AUTHOR'S NOTE

Optical methods to visualize membrane potential dynamics provide a powerful complement to  $\text{Ca}^{2+}$  imaging, patch clamp electrophysiology, and multi-electrode array (MEA) recordings. However, modern voltage imaging strategies often require complicated optics, custom-built microscopes, or genetic manipulations that are impractical outside of a subset of model organisms. Here, we describe the use of Berkeley Red Sensor of Transmembrane potential, or BeRST 1, a far-red voltage-sensitive fluorophore that can directly visualize membrane potential changes with millisecond resolution across dozens of neurons. Using only commercially available components, voltage imaging with BeRST 1 reveals profound changes in neuronal connectivity during development, exposes changes to firing rate during acute pharmacological perturbation, and illuminates

substantial increases in network connectivity in response to chronic exposure to amyloid beta.

## DATA AVAILABILITY STATEMENT

The raw data supporting the conclusions of this article will be made available by the authors, without undue reservation.

## AUTHOR CONTRIBUTIONS

AW conceived, designed, and conducted the experiments, wrote, and edited the manuscript. BR conducted the experiments, contributed to the figures, and edited the manuscript. KK, PZ, and KS contributed to the analysis and code. EM conceived and designed the experiments, wrote, and edited the manuscript. All authors contributed to the article and approved the submitted version.

## FUNDING

We acknowledge support from the NIH (NS098088). BR was supported in part by an NIH Training Grant (T32GM066698).

## SUPPLEMENTARY MATERIAL

The Supplementary Material for this article can be found online at: <https://www.frontiersin.org/articles/10.3389/fnins.2021.643859/full#supplementary-material>

**Supplementary Figure 1** | Optimization of BeRST 1 light power. Representative raw fluorescence traces normalized to baseline fluorescence values during a 30 s imaging bout used to score neurons as (a) healthy or (b) unhealthy. Neurons scored as (a) healthy have just a single, linear baseline, while neurons scored as (b) unhealthy have a change in the slope of the baseline (upper and middle trace), non-linear rises in baseline (middle trace), or abrupt steps in the baseline (lower trace). (c) Plot of the fluorescence intensity of the baseline for neurons characterized as either healthy or unhealthy at 500 nM or 1  $\mu\text{M}$  BeRST 1 dye loading. Each point represents the baseline fluorescence intensity of a single neuron. Bars plot shows the mean fluorescence intensity and error bars are  $\pm$  standard error of the mean. (d) Plot of fraction of healthy neurons (%) vs. illumination intensity. At lower BeRST 1 concentrations (500 nM, blue), higher light intensities (up to 31  $\text{mW}/\text{mm}^2$ ) could be used without any signs of unhealthy neurons (as defined above). At higher concentrations of BeRST 1 (1  $\mu\text{M}$ , red), lower light intensities had to be used (<17  $\text{mW}/\text{mm}^2$ ) to avoid unhealthy neurons. Numbers next to data points are the number of neurons analyzed. (e) Plot of SNR per AP vs. relative fluorescence intensity for BeRST 1 loading at 500 nM (circles) and 1  $\mu\text{M}$  (triangles), using between 6.5 and 70  $\text{mW}/\text{mm}^2$  excitation power (same excitation light power scale as in "c").

## REFERENCES

- Abdelfattah, A. S., Kawashima, T., Singh, A., Novak, O., Liu, H., Shuai, Y., et al. (2019). Bright and photostable chemigenetic indicators for extended *in vivo* voltage imaging. *Science* 365, 699–704. doi: 10.1126/science.aav6416
- Abramov, E., Dolev, I., Fogel, H., Ciccotosto, G. D., Ruff, E., and Slutsky, I. (2009). Amyloid-beta as a positive endogenous regulator of release probability at hippocampal synapses. *Nat. Neurosci.* 12, 1567–1576. doi: 10.1038/nn.2433

- Adil, M. M., Rodrigues, G. M. C., Kulkarni, R. U., Rao, A. T., Chernavsky, N. E., Miller, E. W., et al. (2017a). Efficient generation of hPSC-derived midbrain dopaminergic neurons in a fully defined, scalable, 3D biomaterial platform. *Sci. Rep.* 7:40573.
- Adil, M. M., Vazin, T., Ananthanarayanan, B., Rodrigues, G. M. C., Rao, A. T., Kulkarni, R. U., et al. (2017b). Engineered hydrogels increase the post-transplantation survival of encapsulated hESC-derived midbrain dopaminergic neurons. *Biomaterials* 136, 1–11. doi: 10.1016/j.biomaterials.2017.05.008

- Basarsky, T., Parpura, V., and Haydon, P. (1994). Hippocampal synaptogenesis in cell culture: developmental time course of synapse formation, calcium influx, and synaptic protein distribution. *J. Neurosci.* 14, 6402–6411. doi: 10.1523/jneurosci.14-11-06402.1994
- Brewer, G. J., Torricelli, J. R., Evege, E. K., and Price, P. J. (1993). Optimized survival of hippocampal neurons in B27-supplemented neurobasal™, a new serum-free medium combination. *J. Neurosci. Res.* 35, 567–576. doi: 10.1002/jnr.490350513
- Buchanan, E. K., Kinsella, I., Zhou, D., Zhu, R., Zhou, P., Gerhard, F., et al. (2019). Penalized matrix decomposition for denoising, compression, and improved demixing of functional imaging data. *BioRxiv* [Preprint] bioRxiv:334706
- Burrone, J., O'Byrne, M., and Murthy, V. N. (2002). Multiple forms of synaptic plasticity triggered by selective suppression of activity in individual neurons. *Nature* 420, 414–418. doi: 10.1038/nature01242
- Busche, M. A., Chen, X., Henning, H. A., Reichwald, J., Staufenbiel, M., Sakmann, B., et al. (2012). Critical role of soluble amyloid- $\beta$  for early hippocampal hyperactivity in a mouse model of Alzheimer's disease. *Proc. Natl. Acad. Sci. U.S.A.* 109, 8740–8745. doi: 10.1073/pnas.1206171109
- Cai, C., Friedrich, J., Pnevmatikakis, E. A., Podgorski, K., and Giovannucci, A. (2020). VolPy: automated and scalable analysis pipelines for voltage imaging datasets. *BioRxiv* [Preprint] bioRxiv:2020.2001.2002.892323
- Chang, E. F. (2015). Towards large-scale, human-based, mesoscopic neurotechnologies. *Neuron* 86, 68–78. doi: 10.1016/j.neuron.2015.03.037
- Ciccone, R., Franco, C., Piccialli, I., Boscia, F., Casamassa, A., de Rosa, V., et al. (2019). Amyloid  $\beta$ -Induced upregulation of Na(v)1.6 underlies neuronal hyperactivity in Tg2576 Alzheimer's disease mouse model. *Sci. Rep.* 9:13592.
- Cutts, C. S., and Eglén, S. J. (2014). Detecting pairwise correlations in spike trains: an objective comparison of methods and application to the study of retinal waves. *J. Neurosci.* 34, 14288–14303. doi: 10.1523/jneurosci.2767-14.2014
- Deal, P. E., Liu, P., Al-Abdullatif, S. H., Muller, V. R., Shamardani, K., Adesnik, H., et al. (2020). Covalently tethered rhodamine voltage reporters for high speed functional imaging in brain tissue. *J. Am. Chem. Soc.* 142, 614–622. doi: 10.1021/jacs.9b12265
- Dotti, C., Sullivan, C., and Banker, G. (1988). The establishment of polarity by hippocampal neurons in culture. *J. Neurosci.* 8, 1454–1468. doi: 10.1523/jneurosci.08-04-01454.1988
- Elman, J. A., Oh, H., Madison, C. M., Baker, S. L., Vogel, J. W., Marks, S. M., et al. (2014). Neural compensation in older people with brain amyloid- $\beta$  deposition. *Nat. Neurosci.* 17, 1316–1318. doi: 10.1038/nn.3806
- Farrant, M., and Nusser, Z. (2005). Variations on an inhibitory theme: phasic and tonic activation of GABA receptors. *Nat. Rev. Neurosci.* 6, 215–229. doi: 10.1038/nrn1625
- Fiala, T., Wang, J., Dunn, M., Šebej, P., Choi, S. J., Nwadiabia, E. C., et al. (2020). Chemical targeting of voltage sensitive dyes to specific cells and molecules in the brain. *J. Am. Chem. Soc.* 142, 9285–9301. doi: 10.1021/jacs.0c00861
- Frady, E. P., Kapoor, A., Horvitz, E., and Kristan, W. B. Jr. (2016). Scalable semisupervised functional neurocartography reveals canonical neurons in behavioral networks. *Neural Comput.* 28, 1453–1497. doi: 10.1162/neco\_a\_00852
- Furshpan, E. J., and Potter, D. D. (1989). Seizure-like activity and cellular damage in rat hippocampal neurons in cell culture. *Neuron* 3, 199–207. doi: 10.1016/0896-6273(89)90033-0
- Goda, Y., and Davis, G. W. (2003). Mechanisms of synapse assembly and disassembly. *Neuron* 40, 243–264. doi: 10.1016/s0896-6273(03)00608-1
- Gong, Y., Huang, C., Li, J. Z., Grewe, B. F., Zhang, Y., Eismann, S., et al. (2015). High-speed recording of neural spikes in awake mice and flies with a fluorescent voltage sensor. *Science* 350, 1361–1366. doi: 10.1126/science.aab0810
- Grabrucker, A., Vaida, B., Bockmann, J., and Boeckers, T. M. (2009). Synaptogenesis of hippocampal neurons in primary cell culture. *Cell Tissue Res.* 338, 333–341. doi: 10.1007/s00441-009-0881-z
- Grenier, V., Daws, B. R., Liu, P., and Miller, E. W. (2019). Spying on neuronal membrane potential with genetically targetable voltage indicators. *J. Am. Chem. Soc.* 141, 1349–1358. doi: 10.1021/jacs.8b11997
- Hablitz, J. J. (1984). Picrotoxin-induced epileptiform activity in hippocampus: role of endogenous versus synaptic factors. *J. Neurophysiol.* 51, 1011–1027. doi: 10.1152/jn.1984.51.5.1011
- Hill, E. S., Moore-Kochlacs, C., Vasireddi, S. K., Sejnowski, T. J., and Frost, W. N. (2010). Validation of independent component analysis for rapid spike sorting of optical recording data. *J. Neurophysiol.* 104, 3721–3731. doi: 10.1152/jn.00691.2010
- Hochbaum, D. R., Zhao, Y., Farhi, S. L., Klapoetke, N., Werley, C. A., Kapoor, V., et al. (2014). All-optical electrophysiology in mammalian neurons using engineered microbial rhodopsins. *Nat. Methods* 11, 825–833. doi: 10.1038/nmeth.3000
- Huang, Y. L., Walker, A. S., and Miller, E. W. (2015). A photostable silicon rhodamine platform for optical voltage sensing. *J. Am. Chem. Soc.* 137, 10767–10776. doi: 10.1021/jacs.5b06644
- Huijbers, W., Mormino, E. C., Schultz, A. P., Wigman, S., Ward, A. M., Larvie, M., et al. (2015). Amyloid- $\beta$  deposition in mild cognitive impairment is associated with increased hippocampal activity, atrophy and clinical progression. *Brain* 138, 1023–1035. doi: 10.1093/brain/awv007
- Hyvärinen, T., Hyysalo, A., Kapucu, F. E., Aarnos, L., Vinogradov, A., Eglén, S. J., et al. (2019). Functional characterization of human pluripotent stem cell-derived cortical networks differentiated on laminin-521 substrate: comparison to rat cortical cultures. *Sci. Rep.* 9:17125.
- Jin, L., Han, Z., Platisa, J., Wooltorton Julian, R. A., Cohen Lawrence, B., and Pieribone Vincent, A. (2012). Single action potentials and subthreshold electrical events imaged in neurons with a fluorescent protein voltage probe. *Neuron* 75, 779–785. doi: 10.1016/j.neuron.2012.06.040
- Kiselev, V. Y., Andrews, T. S., and Hemberg, M. (2019). Challenges in unsupervised clustering of single-cell RNA-seq data. *Nat. Rev. Genet.* 20, 273–282. doi: 10.1038/s41576-018-0088-9
- Kubista, H., Boehm, S., and Hotka, M. (2019). The paroxysmal depolarization shift: reconsidering its role in epilepsy, epileptogenesis and beyond. *Int. J. Mol. Sci.* 20:577. doi: 10.3390/ijms20030577
- Kulkarni, R. U., and Miller, E. W. (2017). Voltage imaging: pitfalls and potential. *Biochemistry* 56, 5171–5177. doi: 10.1021/acs.biochem.7b00490
- Kulkarni, R. U., Yin, H., Pourmandi, N., James, F., Adil, M. M., Schaffer, D. V., et al. (2017). A rationally designed, general strategy for membrane orientation of photoinduced electron transfer-based voltage-sensitive dyes. *ACS Chem. Biol.* 12, 407–413. doi: 10.1021/acscchembio.6b00981
- Lin, M. Z., and Schnitzer, M. J. (2016). Genetically encoded indicators of neuronal activity. *Nat. Neurosci.* 19, 1142–1153. doi: 10.1038/nn.4359
- Liu, P., Grenier, V., Hong, W., Muller, V. R., and Miller, E. W. (2017). Fluorogenic targeting of voltage-sensitive dyes to neurons. *J. Am. Chem. Soc.* 139, 17334–17340. doi: 10.1021/jacs.7b07047
- Liu, P., and Miller, E. W. (2020). Electrophysiology, unplugged: imaging membrane potential with fluorescent indicators. *Acc. Chem. Res.* 53, 11–19. doi: 10.1021/acs.accounts.9b00514
- MacQueen, J. (1967). "Some methods for classification and analysis of multivariate observations," in *Proceedings of the 5th Berkeley Symposium on Mathematical Statistics and Probability*, Vol. 1, (Berkeley, CA: University of California Press), 281–297.
- Miller, E. W., Lin, J. Y., Frady, E. P., Steinbach, P. A., Kristan, W. B. Jr., and Tsien, R. Y. (2012). Optically monitoring voltage in neurons by photo-induced electron transfer through molecular wires. *Proc. Natl. Acad. Sci. U.S.A.* 109, 2114–2119. doi: 10.1073/pnas.1120694109
- Moffat, J. G., Vincent, F., Lee, J. A., Eder, J., and Prunotto, M. (2017). Opportunities and challenges in phenotypic drug discovery: an industry perspective. *Nat. Rev. Drug Discov.* 16, 531–543. doi: 10.1038/nrd.2017.111
- Newland, C. F., and Cull-Candy, S. G. (1992). On the mechanism of action of picrotoxin on GABA receptor channels in dissociated sympathetic neurones of the rat. *J. Physiol.* 447, 191–213. doi: 10.1113/jphysiol.1992.sp018998
- Nguyen, C., Upadhyay, H., Murphy, M., Borja, G., Rozsahegyi, E. J., Barnett, A., et al. (2019). Simultaneous voltage and calcium imaging and optogenetic stimulation with high sensitivity and a wide field of view. *Biomed. Opt. Express* 10, 789–806. doi: 10.1364/boe.10.000789
- Ortiz, G., Liu, P., Naing, S. H. H., Muller, V. R., and Miller, E. W. (2019). Synthesis of sulfonated carbofluoresceins for voltage imaging. *J. Am. Chem. Soc.* 141, 6631–6638. doi: 10.1021/jacs.9b01261
- Ovsepian, S. V. (2019). The dark matter of the brain. *Brain Struct. Funct.* 224, 973–983. doi: 10.1007/s00429-019-01835-7
- Palop, J. J., Chin, J., Roberson, E. D., Wang, J., Thwin, M. T., Bien-Ly, N., et al. (2007). Aberrant excitatory neuronal activity and compensatory remodeling of inhibitory hippocampal circuits in mouse models of Alzheimer's disease. *Neuron* 55, 697–711. doi: 10.1016/j.neuron.2007.07.025

- Palop, J. J., and Mucke, L. (2016). Network abnormalities and interneuron dysfunction in Alzheimer disease. *Nat. Rev. Neurosci.* 17, 777–792. doi: 10.1038/nrn.2016.141
- Peña, F., Gutiérrez-Lerma, A., Quiroz-Baez, R., and Arias, C. (2006). The role of beta-amyloid protein in synaptic function: implications for Alzheimer's disease therapy. *Curr. Neuropharmacol.* 4, 149–163. doi: 10.2174/157015906776359531
- Piatkevich, K. D., Jung, E. E., Straub, C., Linghu, C., Park, D., Suk, H. J., et al. (2018). A robotic multidimensional directed evolution approach applied to fluorescent voltage reporters. *Nat. Chem. Biol.* 14, 352–360. doi: 10.1038/s41589-018-0004-9
- Puppo, F., Sadegh, S., Trujillo, C. A., Thunemann, M., Campbell, E., Vandenberghe, M., et al. (2021). All-optical electrophysiology in hiPSC-derived neurons with synthetic voltage sensors. *bioRxiv* [Preprint] biorxiv:2021.2001.2018.427081
- Reich, D. S., Mechler, F., Purpura, K. P., and Victor, J. D. (2000). Interspike intervals, receptive fields, and information encoding in primary visual cortex. *J. Neurosci.* 20, 1964–1974. doi: 10.1523/jneurosci.20-05-01964.2000
- Rodrigues, G. M. C., Gaj, T., Adil, M. M., Wahba, J., Rao, A. T., Lorbeer, F. K., et al. (2017). Defined and scalable differentiation of human oligodendrocyte precursors from pluripotent stem cells in a 3D culture system. *Stem Cell Rep.* 8, 1770–1783. doi: 10.1016/j.stemcr.2017.04.027
- Shankar, G. M., and Walsh, D. M. (2009). Alzheimer's disease: synaptic dysfunction and A $\beta$ . *Mol. Neurodegener.* 4:48.
- Sperling, R. A., Laviolette, P. S., O'Keefe, K., O'Brien, J., Rentz, D. M., Pihlajamaki, M., et al. (2009). Amyloid deposition is associated with impaired default network function in older persons without dementia. *Neuron* 63, 178–188. doi: 10.1016/j.neuron.2009.07.003
- Stine, W. B., Dahlgren, K. N., Krafft, G. A., and LaDu, M. J. (2003). *In vitro* characterization of conditions for amyloid- $\beta$  peptide oligomerization and fibrillogenesis. *J. Biol. Chem.* 278, 11612–11622. doi: 10.1074/jbc.M210207200
- St-Pierre, F., Marshall, J. D., Yang, Y., Gong, Y., Schnitzer, M. J., and Lin, M. Z. (2014). High-fidelity optical reporting of neuronal electrical activity with an ultrafast fluorescent voltage sensor. *Nat. Neurosci.* 17, 884–889. doi: 10.1038/nn.3709
- Südhof, T. C. (2018). Towards an understanding of synapse formation. *Neuron* 100, 276–293. doi: 10.1016/j.neuron.2018.09.040
- Sundukova, M., Prifti, E., Bucci, A., Kirillova, K., Serrao, J., Reymond, L., et al. (2019). A chemogenetic approach for the optical monitoring of voltage in neurons. *Angew. Chem. Int. Ed.* 58, 2341–2344. doi: 10.1002/anie.201812967
- Turrigiano, G. G., Leslie, K. R., Desai, N. S., Rutherford, L. C., and Nelson, S. B. (1998). Activity-dependent scaling of quantal amplitude in neocortical neurons. *Nature* 391, 892–896. doi: 10.1038/36103
- Vedunova, M., Sakharnova, T., Mitroshina, E., Perminova, M., Pimashkin, A., Zakharov, Y., et al. (2013). Seizure-like activity in hyaluronidase-treated dissociated hippocampal cultures. *Front. Cell. Neurosci.* 7:149. doi: 10.3389/fncel.2013.00149
- Verret, L., Mann Edward, O., Hang Giao, B., Barth Albert, M. I., Cobos, I., Ho, K., et al. (2012). Inhibitory interneuron deficit links altered network activity and cognitive dysfunction in Alzheimer model. *Cell* 149, 708–721. doi: 10.1016/j.cell.2012.02.046
- Wagenaar, D. A., Pine, J., and Potter, S. M. (2006). An extremely rich repertoire of bursting patterns during the development of cortical cultures. *BMC Neurosci.* 7:11. doi: 10.1186/1471-2202-7-11
- Walker, A. S., Raliski, B. K., Nguyen, D. V., Zhang, P., Sanders, K., Karbasi, K., et al. (2021). Imaging voltage in complete neuronal networks within patterned microislands reveals preferential wiring of excitatory hippocampal neurons. *Front. Neurosci.* doi: 10.3389/fnins.2021.643868
- Wang, Z., Jackson, R. J., Hong, W., Taylor, W. M., Corbett, G. T., Moreno, A., et al. (2017). Human brain-derived A $\beta$  oligomers bind to synapses and disrupt synaptic activity in a manner that requires APP. *J. Neurosci.* 37, 11947–11966. doi: 10.1523/jneurosci.2009-17.2017
- Werley, C. A., Brookings, T., Upadhyay, H., Williams, L. A., McManus, O. B., and Dempsey, G. T. (2017a). All-Optical electrophysiology for disease modeling and pharmacological characterization of neurons. *Curr. Protoc. Pharmacol.* 78, 11.20.11–11.20.24.
- Werley, C. A., Chien, M.-P., and Cohen, A. E. (2017b). Ultrawidefield microscope for high-speed fluorescence imaging and targeted optogenetic stimulation. *Biomed. Opt. Express* 8, 5794–5813. doi: 10.1364/boe.8.005794
- Williams, L. A., Joshi, V., Murphy, M., Ferrante, J., Werley, C. A., Brookings, T., et al. (2019). Scalable measurements of intrinsic excitability in human iPSC cell-derived excitatory neurons using all-optical electrophysiology. *Neurochem. Res.* 44, 714–725. doi: 10.1007/s11064-018-2694-5
- Williams Megan, E., Wilke Scott, A., Daggett, A., Davis, E., Otto, S., Ravi, D., et al. (2011). Cadherin-9 regulates synapse-specific differentiation in the developing hippocampus. *Neuron* 71, 640–655. doi: 10.1016/j.neuron.2011.06.019
- Woodford, C. R., Frady, E. P., Smith, R. S., Morey, B., Canzi, G., Palida, S. F., et al. (2015). Improved PeT molecules for optically sensing voltage in neurons. *J. Am. Chem. Soc.* 137, 1817–1824. doi: 10.1021/ja510602z
- Xie, M. E., Adam, Y., Fan, L. Z., Böhm, U. L., Kinsella, I., Zhou, D., et al. (2020). High fidelity estimates of spikes and subthreshold waveforms from 1-photon voltage imaging *in vivo*. *bioRxiv* [Preprint] bioRxiv:2020.2001.2026.920256
- Xu, D., and Tian, Y. (2015). A comprehensive survey of clustering algorithms. *Ann. Data Sci.* 2, 165–193. doi: 10.1007/s40745-015-0040-1
- Yan, P., Acker, C. D., Zhou, W.-L., Lee, P., Bollensdorff, C., Negrean, A., et al. (2012). Palette of fluorinated voltage-sensitive hemicyanine dyes. *Proc. Natl. Acad. Sci. U.S.A.* 109, 20443–20448. doi: 10.1073/pnas.1214850109
- Yuste, R. (2015). From the neuron doctrine to neural networks. *Nat. Rev. Neurosci.* 16, 487–497. doi: 10.1038/nrn3962
- Zott, B., Simon, M. M., Hong, W., Unger, F., Chen-Engerer, H. J., Frosch, M. P., et al. (2019). A vicious cycle of  $\beta$  amyloid-dependent neuronal hyperactivation. *Science* 365, 559–565. doi: 10.1126/science.aay0198

**Conflict of Interest:** EM and AW are listed as inventors on a patent application filed by the Regents of the University of California describing “long wavelength voltage sensitive dyes.”

The remaining authors declare that the research was conducted in the absence of any commercial or financial relationships that could be construed as a potential conflict of interest.

Copyright © 2021 Walker, Raliski, Karbasi, Zhang, Sanders and Miller. This is an open-access article distributed under the terms of the Creative Commons Attribution License (CC BY). The use, distribution or reproduction in other forums is permitted, provided the original author(s) and the copyright owner(s) are credited and that the original publication in this journal is cited, in accordance with accepted academic practice. No use, distribution or reproduction is permitted which does not comply with these terms.